Joining of AA5052 to CF/PEEK by friction lap welding

Jamal Sheikh-Ahmad, Redouane Zitoune, Claire Morel, Jean-François Ferrero, Benoit Vieille

Joining of AA5052 to CF/PEEK by friction lap welding

Jamal Sheikh-Ahmad

jamal.sheikh-ahmad@wne.edu

Western New England University https://orcid.org/0000-0003-3537-0311

Redouane Zitoune
Claire Morel
Jean-François Ferrero
Benoit Vieille

Research Article

Keywords: Friction lap welding, hybrid structures, AA5052, PEEK-CFRP, interface temperatures, lap shear strength.

Posted Date: November 20th, 2023

DOI: https://doi.org/10.21203/rs.3.rs-3601965/v1

Version of Record: A version of this preprint was published at The International Journal of Advanced Manufacturing Technology on March 19th, 2024. See the published version at https://doi.org/10.1007/s00170-024-13457-3.

Abstract

The joining of aluminum alloy AA5052 and carbon fiber reinforced polyether ether ketone (CF/PEEK) by friction lap welding was investigated under different conditions of surface texturing and process temperatures. The joint quality was evaluated by measurement of the tensile shear force and examination of the joint morphology. The welding experiments were conducted under different tool rotational speeds for two types of surface texturing of the aluminum alloy, namely mechanical engraving and sand blasting. The temperatures across the weld line were measured during the process of welding using thermocouples mounted at specific locations, and the temperature distribution at the interface was determined by an inverse heat conduction method. It was found that the temperatures at the interface exceeded the melting temperature of PEEK for all testing conditions, but was always below PEEK thermal degradation temperature. It was also found that joint performance of mechanically engraved samples increased with increasing the interface temperatures. This was attributed to the increased mechanical interlocking due to the flow of melted PEEK into surface features of the engraved sample. The joint strength of sand blasted samples did not change considerably with interface temperatures.

Introduction

Hybrid structures made by combining dissimilar materials such as polymers to polymers, polymers to metals and polymer composites to metals in single sub-assemblies are replacing traditional assemblies of these materials typically made by joining separate parts. The driving philosophy of hybrid structures is to enhance product design flexibility, allowing the differing materials to be utilized in an efficient and functional manner based on the specific properties of the individual materials. Currently, polymer-metal hybrids are replacing metal structures in automotive front-end modules, instrument-panel and bumper cross-beams, door modules, and tailgate applications (Grujicic et al., 2008). Polymer composite metal hybrids (stacks) are similarly finding increased utilization in modern aircraft structures such as the Boeing 787 and the Airbus 380 (Mouritz, 2012).

The fabrication of large and complex hybrid structures usually requires joining. The most frequent methods used are mechanical fastening, adhesive bonding, injection over-molding and hybrid joining, e.g. fastening combined with bonding (Jiang et al., 2020). However, these methods present several limitations, such as the need to drill holes and the associated stress concentration, extra weight, the demand for extensive surface preparation, size and complexity limitations and harmful environmental emissions. To avoid these problems, emerging joining techniques such as ultrasonic welding, laser welding, friction stir welding and friction lap welding have been proposed and researched recently.

A few studies investigated the joining of fiber reinforced thermoplastic polymer composites (FRTPs) to metals by friction stir spot welding, friction stir lap welding and friction lap welding. Huang et al. (2018) studied the friction stir lap welding of short carbon fiber-PEEK and AA2060 with a tool with stationary shoulder and rotating tapered pin. They concluded that the primary joining mechanisms were macro/micro-mechanical interlocking, the chemical bond and the partial infiltration of the carbon fiber

into the Al alloy. Lambiase et al. (2021) investigated the joining of AA7075 with carbon fiber reinforced thermoplastic CFRTP in a spot welding arrangement. Laser texturing of the surface of the aluminum sample was employed to enhance mechanical interlocking. It was concluded that joining is feasible only for textured aluminum samples. Similarly, Ota et al. (2021) utilized friction stir spot welding to join CFRTP to aluminum alloy 6061. Surface treatment of the aluminum alloy included etching by HCl and silanization. It was concluded that the interfacial strength of the joint was improved significantly by surface treatment through mechanical interlocking and chemical bonding. Dong et al. (2021) investigated the joining of AA5052 and carbon fiber reinforced PEEK by friction stir spot welding. For this work, the aluminum alloy surface was treated by sand blasting before welding. They concluded that the main joining mechanisms included adhesion and mechanical interlocking. Han et al. (2020) and Wang et al. (2021) have also demonstrated that surface texturing was key to improving the joint performance in friction stir welding of metal to polymer and polymer composites. Li et al. (2021) showed that the joint strength in friction lap welding of short fiber reinforced PEEK and aluminum alloy AA7075 can be improved by applying heat on the top surface of the aluminum sheet. This heating allowed better penetration of the molten PEEK into the textured aluminum sheet surface.

Even though most of the studies above emphasized the role of mechanical interlocking by creating surface textures on the metal part, other studies in the literature argued for the important role of chemical bonding, as a secondary joining mechanism in dissimilar joining of FRTPs and metals. The evidence of chemical bonding was implied by the presence of chemical compounds C-O-M at the interfaces, where M refers to alloying elements of the metallic parts, such as Al and Mg These compounds form at high temperatures by the reaction between the carbonyl group C = O on the polymer surface and the metal oxide on the metal surface (Liu, 2018). Nagatsuka et al. (2015) performed friction lap welding of AA5052 and SCF-PA6and concluded, based on XPS analysis that joining occurred by MgO formation. Sanding of the metal surface increased the joint strength from 1.0 to 2.9 kN, a significant improvement due to micro-interlocking. Wu et al. (2018) performed friction lap joining of oxygen free high conductivity copper and SCF-PA6. It was argued that chemical bonding was the main reason for joint strength due to formation of hydrogen bonding between PA6 and Cu_2O on the Cu surface. Wang et al. (2022) utilized laser ablation and Wang et al. (2023) utilized a combination of hot water treatment followed by laser ablation to enhance chemical bonding. It was shown that the tensile strength increased from 24.48 MPa to 30.2 MPa due to this enhancement brought about by the formation of C-O-Al bonds. Sandeep et al. (2023) also reported the formation of C-O-Al in the friction lap welding of AA7475 and PPS. The lapjoint shear strength reported was 16.8 MPa.

The studies in the literature indicate that mechanical interlocking is the primary joining mechanism, which can be enhanced by chemical bonding. The role of process temperatures in both mechanisms is important. The softening of the polymer resin and subsequent melting and flow into the microstructures created on the metal surface is key to the formation of strong mechanical bonds. In the present study, the effect of the surface texturing and the process temperatures on the joint performance of friction lap joint between aluminum alloy AA5052 and composite part (CF/PEEK) is investigated. For this, two types of

surface texturing are considered, which are mechanical engraving and sand blasting. Process temperatures were manipulated by varying the tool rotational speed, and were investigated by temperature measurement and numerical simulation. Lap joint strength was determined by ASTM D1002 tensile shear test and joint morphology was investigated by scanning electron microscopy and X-ray tomography.

Materials and Methods

The carbon fiber reinforced PEEK (CF/PEEK) was received as 7 plies satin weave laminate with fiber content of 50% and a thickness of 2.2mm. The laminate was cut into 80x100mm^2 blanks. Similar size blanks of AA5052 were also cut from a commercially available 2mm thick sheet. The welding of aluminum alloy AA5052 to CF/PEEK was conducted on a manual milling machine as shown in Fig. 1, and welding took place along the 100 mm side. The welding configuration was friction lap joint, with the aluminum plate placed on top, (Fig. 1(a)). The aluminum sheet was placed on the advancing side and the CF/PEEK was placed on the retreating side for all experiments. The lap joint width was 15mm. Prior to assembly, the aluminum surface was cleaned by alcohol to remove contaminants. The rotational speed was varied, while the welding speed and tilt angle were held constant at 40 mm/min and 0 degrees, respectively. The plunge depth was approximately 0.5mm from the surface of the aluminum sheet. The welding tool was a pin-less cylindrical type shoulder made of carbon steel. The tool shoulder in contact with the workpiece has a diameter of 15 mm and a 1mm radius groove machined at an intermediate radius on the face of the shoulder as shown in Fig. 1(b). Different surface preparations of the aluminum alloy sheets were introduced to improve the mechanical interlocking between the two dissimilar materials, namely surface texturing with sand blasting (SB) and engraving were utilized. The sandblasting pretreatment was applied by a commercial vendor. The grit size of sandblasting particles was 80 and the sandblasting time was 5 seconds. Engraving (dots) consisted of 0.5mm deep dots at 1mm spacing embossed on the lap joint area. Before welding the surface texture was characterized by means of 3D optical profilometer (Infinite Focus G5 from Alicona) which is based on non-contact measurement. Figure 2 shows the surface textures of the sand-blasted and engraved surfaces. The engraving treatment created conical holes with burr of flash at their brims, and the burr height was in the order of 100 µm. Table 1 shows the arithmetic area roughness S_a and maximum peak to valley height S_z for the two samples. Table 2 shows the combination of experimental parameters considered in this study.

Table 1
Area roughness measurements of the untreated and treated AA plates.

	As received	SB	Dots
Sa (µm)	1.70	13.36	76.85
Sz (µm)	53.58	201.38	638.71

Table 2
FLW process parameters. Welding speed is 40 mm/min, plunge depth is approximately 0.5mm and tilt angle is 0° for all conditions.

Run	1	2	3	4	5	6	7
Rotation speed (rpm)	770	949	949	949	1090	949	1090
Surface prep	SB	SB	Dots	None	SB	Dots	None

Welding temperatures were measured using type K thermocouples at four locations across the weld line as shown in Fig. 1(a). Points A and B were on the aluminum side, approximately 13mm and 9mm from the weld line, respectively. Points C and D were on the CF/PEEK side approximately 9mm and 13mm from the weld line, respectively. Shallow holes of 1mm diameter were drilled for thermocouple placement. The holes were filled with thermal conductive paste, then the thermocouples were inserted and secured by an adhesive tape. Pico TC-08 temperature logger was used to record the thermocouple measurements at frequency of 1/s.

The lap joint strength was evaluated by conducting tensile shear tests according to ASTM D1002 standard. Two tensile specimens 25mm wide and 145mm long were cut from each welded assembly, perpendicular to the weld line and taps were glued at both ends to avoid bending during tensile testing. Tensile shear tests were carried out on a 810 Material Testing System (MTS) at the crosshead speed of 0.5 mm/min. The maximum load before joint separation was recorded for each test and the average from the two specimens was calculated. The macrostructure and microstructure of the joint interfaces were investigated using confocal and scanning electron microscopy. The microstructure at the interface of the lap joint was analyzed using Quanta 250 ESEM with a beam acceleration voltage of 5 KV, working distance of 10 mm, and chamber pressure of 10^{-3} Pa. A cross section of the joint was mounted using in epoxy resin, then the surface was ground and polished before SEM examination. The interfaces between the two dissimilar materials were also characterized using X-ray tomography (Nikon XT H 225 X-ray CT scan machine). Segments of the lap joint, approximately 20mm x 20mm were cut from the welded assembly and placed 10 cm from the X-ray source under a voltage of 225 kV and a current of 2000 mA. With this selection of parameters, the average voxel size was 18 μm. Topography and surface texture of the joint interfaces, after separation by tensile testing, were studied using Alicona Infinite Focus G5 microscope.

Numerical Model

The heat conduction problem into the workpiece during friction lap welding was solved numerically by an iterative inverse method using Abaqus. Figure 3 shows a schematic of the numerical heat transfer model where the heat flux from friction under the tool shoulder (q_s) is represented by a moving heat source with speed (v) equivalent to the welding speed. The surface heat flux was distributed linearly over the contact area between the rotating shoulder and the workpiece according to the equation,

$$q_s = q_o r 0 \le r \le r_o$$

1

where q_o is the heat flux amplitude, r is the radial distance from the tool center and r_o is the radius of the tool shoulder. In a lap joint, heat from friction conducts through the thickness of the aluminum workpiece, through a gap and into the CF/PEEK workpiece. Hence, a gap conductance between the AA and CF/PEEK mating surfaces is defined in the numerical model. In this model, the gap conductance was assumed to have different values in different regions of the lap joint as shown in Fig. 4. K1 was defined in the welded interface, K2 was defined at the interface directly under the tool and K3 was defined in the unwelded region of the interface. The approximate values of these conductances were also determined by iteration using the inverse heat conduction approach.

In an inverse heat conduction problem, the magnitude of the heat flux amplitude and gap conductance were determined by minimizing an objective function given by,

$$f = \sum_{i=1}^{n} \left(T_i^s - T_i^{exp} \right)^2$$

2

where T_i^{exp} is the experimentally measured temperature and T_i^s is the simulated temperature at boundary location i. In the iterative solution, the heat flux amplitude and conductances are given initial values and the direct heat conduction problem (Eq. 3) is solved numerically. In this equation, k is thermal conductivity, Q is internal heat generation, which is not present in this study, ρ is density, c is specific heat and t is time.

$$\nabla \bullet k \nabla T + Q = \rho c \frac{\partial T}{\partial t}$$

3

The objective function (Eq. 2) is then evaluated and the solution is repeated by incrementing the heat flux amplitude and conductances, one at a time. This iterative process is terminated when the objective function attains a minimum. The boundary temperatures used for comparison were the top surface temperatures measured at four locations A, B, C and D as shown in Fig. 3.

Figure 5 shows the discretized numerical model with the different mesh sizes in the welding and surrounding regions. The mesh size in the welding and high temperature gradient region was kept at 1x1x1mm^3, while in the regions of low temperature gradient the mesh size was 4x1x1mm^3. The element type used was heat transfer element DC3D8. The total number of elements was 13,600 and the total number of nodes was 21,210. User subroutines DFLUX and GAPCON were implemented in Abaqus for defining the surface heat flux and gap conductance, respectively. Temperature dependent thermal

properties were used in the numerical model. Tables 3 and 4 show the thermal and physical properties of AA5052 and CF/PEEK which were used in the numerical model. Because thermal properties of the CF/PEEK laminate was not available in the literature, these properties were estimated indirectly. Thermal diffusivity, α, across thickness of the laminate was measured as function of temperature in the temperature range from 20 to 200 ^{o}C using laser flash method (Laser Flash Analyzer LFA447 from Netzsch), the data was then extrapolated to higher temperatures. Specific heat was calculated using the law of mixtures from PEEK and carbon data in the literature (Swan et al., 2020). Thermal conductivity across the thickness was calculated from thermal diffusivity, density and specific heat using the equation, $k_y = \alpha \rho c$. Thermal conductivity in the plane direction was estimated numerically using the inverse method. The estimated thermal properties in Table 4 gave good results in the heat conduction analysis.

Table 3
Thermal and physical properties of AA5052 [Zhu and Chao, 2002]

Temperature (°C)	Conductivity (W/m°C)	Specific Heat (J/kg°C)	Density (kg/m^3)
22	168	1056	2700
80	176	1098	2681
180	189	1136	2663
280	203	1176	2644
380	219	1228	2628
480	227	1270	2608

Table 4
Thermal and physical properties of CF/PEEK

Temperature (°C)	Conductivity, k_x, k_z (W/m°C)	Conductivity, k_y (W/m°C)	Specific Heat (J/kg.°C)	Density (kg/m^3)
22	2.34	0.523	898.4	1256
50	2.51	0.541	950.0	
100	2.77	0.559	1053.3	
150	3.02	0.580	1156.5	
200	3.31	0.598	1259.8	
300	3.85	0.637	1466.3	

Results and Discussion

Figure 6 shows a typical lap joint of AA5052 (top, advancing side) and CF/PEEK (bottom, retreating side). The weld line appears relatively smooth, with intermittent gouges due to material removal by the shoulder, and flash on the retreating side. This and similar welded assemblies were cut on a band saw along the dotted lines shown to prepare two tensile lapshear specimens for each test. Each specimen was 25mm wide and 145mm long. The overlap width was 15mm. Below is a discussion of the results of measured and simulated temperatures, joint resistance to separation and joint morphology.

Process Temperatures

Figure 7 shows the simulated temperature distribution in the two joined plates for welding condition 3 (rotation speed of 949 rpm) after 60 seconds. It can be seen that the maximum temperature in the assembly occurs under the tool shoulder in the aluminum workpiece. Furthermore, the heat conducts much more through the metal side than the CF/PEEK side due to the great difference in thermal conductivity. The effect of gap conductance is shown in the differences in heat conduction immediately under the tool, behind the tool and ahead of the tool. The heat conducted into these areas is in direct relationship with the gap conductances in these respective regions. In this particular run, the gap conductances K1, K2 and K3 have the values 8000, 15000 and 300 $W/m^2.K$, respectively.

Figure 8 shows measured and simulated temperatures for thermocouple locations A, B, C and D for run 3. It can be seen that the measured temperatures on the aluminum side are much higher than those on the CF/PEEK side. This is due to the fact that the heat source is generated on top of the aluminum surface and conducts through the metal rapidly as it is evident by the steep heating curve. The temperature at each location increases gradually to a maximum as the tool approaches this location and then gradually decreases due to cooling as the tool moves away. There is an obvious lag in the heating of CF/PEEK due to its low thermal conductivity, as compared to that of AA5052. The maximum temperature on the aluminum side, 9mm from the weld line was 380 ^oC, which is higher than the melting temperature of PEEK, but lower than the thermal degradation temperature. The melting point of PEEK was reported by Dong et al. (2021) to be around 337°C, and thermal degradation occured nearly at 570°C. Visual inspection of the weld line showed melted PEEK squeezing out of the lap joint, which is indicative of the high temperatures in the contact area. It can also be seen from Fig. 8 that the numerical model captures the process temperatures to an acceptable accuracy, where the differences between the measured and simulated peak temperatures were below 8%.

To better understand the material condition at the interface, the simulated temperatures across the weld line halfway from the starting point are plotted as shown in Fig. 9. Figure 9a shows the temperature distribution at the cross section of the lapjoint. It can be seen that the temperature distribution is asymmetrical with respect to the weld line, where higher temperatures occur on the CF/PEEK side due to its lower thermal conductivity. Shallow penetration of the heat into the CF/PEEK sample is also evident since thermal conductivity across the thickness is much smaller than that in the plane direction. This asymmetrical temperature distribution creates asymmetrical melting and material flow on both sides of the weld line. Figure 9b shows the simulated peak temperatures on the surface of the AA5052 and

CF/PEEK materials across the weld line. Superimposed on the same plot are the maximum temperatures measured by the thermocouples at A, B, C and D. The match between measured and simulated peak temperatures indicates that the numerical predictions are accurate. Figure 9b shows that the average peak temperature in the lap joint region is approximately 450 ^{o}C, which is much higher than the melting temperature of PEEK, and could reach the degradation temperature. Table 5 summarizes the average CF/PEEK interface temperatures for all the experiments conducted in this study. Figure 10 shows the simulated CF/PEEK interface temperatures for the different rotation speeds of the welding tool. Indicated with asterisks on the figure are the conditions which produced a successful joint. As can be seen, interfacial temperature alone does not determine the feasibility of the joint, as some conditions with interface temperatures that are above the PEEK melting point did not result in a joint. It can also be seen that no obvious correlation exists between the rotation speed and the average CF/PEEK interface temperature, as this temperature depends both on the heat flux applied on the AA surface (which is a function of the rotation speed), as well as on the gap conductivity, which was determined by an inverse method. Gap conductance depends on many factors, including the pressure at the interface and the surface texture, and its estimated values varied across the different experiments. This variation was most likely due to the rudimentary method of controlling the plunge depth on the milling machine. Variations of the plunge depth from the nominal value of 0.5mm causes variations in the downforce, and hence the gap conductance. As shown in Table 5, the two identical runs 3 and 6 resulted in considerably different CF/PEEK average interface temperatures, most likely due to different plunge depths.

Table 5
Tensile force for separation and average CF/PEEK interface temperature

Run	Rotation Speed (rpm)	Surface Preparation	Average CF/PEEK Temp (^{o}C)	Average Tensile Shear Force (kN)	Average Lap Shear Strength (MPa)
1	770	SB	417	No joint	
2	949	SB	310 (245–350)	1.98	5.3
3	949	Dots	446	2.50	6.7
4	949	None	353	No joint	
5	1090	SB	392	1.83	4.9
6	949	Dots	344	2.19	5.8
7	1090	None	409	No joint	

Joint strength

The lap joint resistance as represented by the maximum tensile shear force obtained before separation of the joined surfaces is shown in Table 5 for the different test conditions. Fracture of the joint occurred at the interface for all test conditions, which suggests that the strength of the joint was determined by the

strength of the interface. As shown, CF/PEEK did not adhere to the aluminum workpiece which did not receive any surface preparation. This is due to the absence of mechanical interlocking as a result of the smooth surface. The maximum shear force was obtained for samples which were engraved by dots. This is understood as the dot engraving provided more anchoring depth and burr features which are not present in the sand blasted samples. The effect of process temperatures on the lap shear force is shown in Fig. 11. The figure shows that the lap joint strength for engraved samples increased by 14% due to increasing the average CF/PEEK temperature at the interface while the sand blasted samples did not benefit from the increased interfacial temperature. This might be explained by the decreased viscosity of the PEEK matrix with increasing temperature and its ability to flow and fill the depressions on the aluminum surface. The surface texture of the engraved aluminum has far more deeper depressions and their filling with molten PEEK would provide higher interlocking forces. The role of processing temperatures in enhancing mechanical interlocking was also emphasized in the study of Correia et al. (2023) in joining glass fiber reinforced (GFR) polymer to AA6082-T6. The maximum lap shear strength obtained in the present study was 6.7 MPa for condition 3. In comparison with different joining methods in the literature, Huang et al. (2018) reported a maximum tensile shear strength of 33 MPa in friction stir lap welding of AA2060-T8 and short carbon fiber reinforced PEEK (SCF/PEEK), Feng et al. (2021) reported a shear strength of 24 MPa in the laser welding of AA6061 and SCF/PEEK, and Bi et al. (2022) reported a tensile shear strength of 19.4 MPa in friction lap welding of AA6061 and CF/PEEK. In all of these studies, the aluminum surface received laser micro-texturing, which proved to be more effective in creating mechanical interlocks than the macro-engraving considered in the present study due to its higher areal density of micro-interlocking features.

Joint morphology

The surfaces of the separated AA5052 and CF/PEEK sheets were inspected using confocal microscope and scanning electron microscope in order to determine the surface texture characteristics. Figure 12 shows the separated AA5052-sandblasted (AA-SB) and CF/PEEK surfaces. It can be seen that the CF/PEEK surface approximately represents a negative of the AA-SB surface. The high region on the right side of the AA-SB surface corresponds to a low region on the left side of the CF/PEEK surface. Comparing area roughness of AA-SB surface with that before welding, it is noted that the arithmetic area roughness Sa has decreased from 13.36 μm to 9.4 μm, which might be attributed to PEEK material filling the pits on the AA surface. Figure 13 shows X-ray scan of the cross section of the joint, which shows the AA material being deformed due to the pressure of the rotating tool. Gouging of the metal surface and rolling of the flash is also obvious. Figure 13b shows a close-up view of the right side of the image where subsurface cracks in the CF/PEEK are visible. Also visible in the image is separation between the two surfaces at the deformed region and at the right corner of the AA part. A visible amount of PEEK which was squeezed out of the joint and solidified on the right side could be recognized. In comparison with Fig. 9a, it is noticed that this phenomenon is associated with the side that has the highest interfacial temperatures. Figure 14 shows a scanning electron microscope image of the interface between the AA5052-SB (top half) and CF/PEEK (bottom half). It is apparent that molten PEEK, which appears as bright regions due to charging,

has filled the depressions in the AA5052-SB surface, which are in the order of 25μm in depth. The presence of voids at the interface is also evident, which might be attributed to incomplete filling of the surface depressions or due to solidification shrinkage. Also seen in the figure are areas of missing PEEK matrix in the top surface of the CF/PEEK laminate. These might indicate the areas where PEEK has been squeezed out of the composite top surface, where interfacial temperatures are the highest.

Figure 15 shows the surface textures of the separated joint of AA-dots and CF/PEEK (run 3). It is evident that some of the engraved holes have been partially filled with molten and solidified PEEK, as indicated by arrows on the figure. Similar to the AA-SB joint surfaces, the CF/PEEK surface is an approximate negative of the AA-dots surface. The high brims around the holes on the AA-dots surface have clearly left their impressions on the CF/PEEK surface. The arithmetic area roughness of the AA-dots has also increased slightly from 76.9 to 72.8 μm after welding. This indicates a minor change in the surface topography after welding and separation. Figure 16 shows an X-ray scan of the cross section of the joint. Deformation of the AA part in this case is more profound than the sand-blasted material due to weakening of the metal part by the engraved dots. In addition, higher stress concentration on the CF/PEEK surface was caused by the engraving, which in turn resulted in a more profound subsurface crack network. The low extent of filling of the engraved holes with molten PEEK is apparent Fig. 16b, where 3 of the holes are only partially filled with molten PEEK. Figure 17 shows scanning electron microscope images of a cross section of the lap joint, with one of the engraved dots in full view. It can be seen that the hole in the AA has been partially filled with AA chips and solidified PEEK. The magnified image in Fig. 17(b) shows the burr at the hole brim forming a hook, which is filled with solidified PEEK. These hooks appear at the brim of all engraved holes and obviously contribute greatly to the mechanical interlocking between AA and PEEK. However, the effectiveness of this macro-interlocking is limited by the amount of PEEK that is squeezed out of the laminate. It is apparent by visual inspection that the volume of engraving is much larger than the amount of PEEK squeezed out, and therefore only partial filling of the holes is possible. In addition, the areal density of the macro-texture features is very small as compared to laser textured surfaces reported in the literature. These two reasons are perhaps the main reasons for the low lap shear strength obtained in the present study, as compared to the lap shear strength of similar joints reported in the literature.

Conclusions

This study considered the effects of mechanical surface texturing and process temperatures on the joint strength of hybrid AA5052-CF/PEEK lap joints fabricated by friction lap welding. The two materials were arranged such that the AA is on the top and on the advancing side, and a pinless rotating tool was used to generate heat and pressure for welding. Two surface pretreatments, namely sand blasting and mechanical engraving were implemented to prepare the metallic surface for welding, and welding runs were conducted at different rotation speeds and fixed welding (traverse) speed. The lapjoint was characterized by mechanical testing, scanning electron microscopy and X-ray tomography. The main conclusions of this study are:

1. Joining by mechanical interlocking is possible when sufficient interlocking features are created on the AA surface, such as in mechanical engraving.

2. High process temperatures are required to melt the PEEK and make it flow into the surface features of the metal part.

3. Joints between engraved AA and CF/PEEK improved by increasing the process temperatures, while joints between sand-blasted AA and CF/PEEK did not. High process temperatures allowed PEEK to flow below metal burrs formed at the hole brim, which formed an anchor for increased mechanical strength.

Declarations

Author Declarations

Availability of data and materials

Data and numerical model associated with this study is available upon request by contacting the corresponding author.

Funding

This work was funded in part by a Competitive Internal Research Award CIRA 2020-084 from Khalifa University of Science and Technology.

Competing Interests

The authors have no conflicts of interest to declare that are relevant to the content of this article.

Author Contributions

All authors contributed to the study conception and design. Material preparation and experiments were performed by Sheikh-Ahmad and Zitoune. Data collection and analysis were performed by Sheikh-Ahmad, Zitoune and Vieille. The first draft of the manuscript was written by Sheikh-Ahmad and Zitoune, and reviewed by Morrel, Ferrero and Vieille. All authors commented on previous versions of the manuscript. All authors read and approved the final manuscript.

References

1. Bi, X., Wang, Z., Xu, M., Li, X. Femtosecond laser fabricated micro/nano interfacial structures to strengthen CFRPEEK/A6061-T6 FLJ hybrid joints. Composites Part B 231 (2022) 109540
2. Correia, A., Santos, P., Braga, D., Cipriano, G., Moreira, P., Infante, V. Effects of processing temperature on failure mechanisms of dissimilar aluminum-to-polymer joints produced by friction stir welding. Engineering Failure Analysis 146 (2023) 107155
3. Dong, H., Tang, Z., Li, P., Wu, B., Hao, X., Ma, C. Friction stir spot welding of 5052 aluminum alloy to carbon fiber reinforced polyether ether ketone composites. Materials and Design 201 (2021) 109495
4. Feng, Z., Ma, G., Su, J., Tan, C., Han, X., Zhao, H., Chen, B., Song, X. Influence of process parameters on the joint characteristics during laser joining of aluminium alloy and CFRTP. Journal of Manufacturing Processes 64 (2021) 1493–1506
5. Grujicic, M., V. Sellappan, M.A. Omar, Norbert Seyr, Andreas Obieglo, Marc Erdmann, Jochen Holzleitner. An overview of the polymer-to-metal direct-adhesion hybrid technologies for load-bearing automotive components. J. Materials Processing Technology 197 (2008) 363–373.
6. Han et al., Achieving a strong polypropylene/aluminum alloy friction spot joint via a surface laser processing pretreatment. Journal of Materials Science & Technology 50 (2020) 103–114
7. Huang et al. Joining of carbon fiber reinforced thermoplastic and metal via friction stir welding with co-controlling shape and performance. Composites Part A 112 (2018) 328–336
8. Jiang, B., Chen, Q, Yang, J. Advances in joining technology of carbon fiber-reinforced thermoplastic composite materials and aluminum alloys. The International Journal of Advanced Manufacturing Technology (2020) 110:2631–2649.
9. Lambiase, F, Paoletti, A., Durante, M. Mechanism of bonding of AA7075 aluminum alloy and CFRP during friction assisted joining. Composite Structures 261 (2021) 113593
10. Li et al, Achieving high-quality metal to polymer-matrix composites joint via top-thermic solid-state lap joining. Composites Part B 219 (2021) 108941
11. Liu, F. C., Dong, P., Lu, W., Sun, K. On formation of Al–O–C bonds at aluminum/polyamide joint interface. Appl. Surf. Sci., vol. 466, no. September 2018, pp. 202–209, 2019, doi: 10.1016/j.apsusc.2018.10.024.
12. Mouritz A.P. (editor) Fibre–polymer composites for aerospace structures and engines, in Introduction to Aerospace Materials, Editor(s): Adrian P. Mouritz, Woodhead Publishing, 2012, Pages 338-393
13. Nagatsuka, K., Yoshida, S., Tsuchiya, A., Nakata, K. Direct joining of carbon-fiber–reinforced plastic to an aluminum alloy using friction lap joining. Composites: Part B 73 (2015) 82–88.
14. Ota et al., Friction stir spot welding of aluminum and carbon fiber reinforced thermoplastic using hybrid surface treatment improving interfacial properties. Materials & Design 212 (2021) 110221
15. Swann, D., Ding, Y., Stoliarov, S. Comparative analysis of pyrolysis and combustion of bisphenol A polycarbonate and poly(ether ether ketone) using two-dimensional modeling: A relation between thermal transport and the physical structure of the intumescent char. Combustion and Flame 212 (2020) 469–485

16. Wang et al., Enhanced aluminum alloy-polymer friction stir welding joints by introducing micro-textures. Materials Letters 295 (2021) 129872
17. Wang, S., Wang, W., Xu, Y., Tian, Y., Zhang, X., Huang, H. Enhancing bonding synergy and mechanical response of metal/composite hybrid joints through physicochemical surface pretreatment. Journal of Materials Processing Tech. 315 (2023) 117923
18. Wang, S., Xu, Y., Wang, W., Tian, Y., Zhang, X., Huang, H., Zheng, D. Enhancing interfacial bonding in friction stir lap welding of light metal and carbon fiber reinforced polymer composite. Journal of Manufacturing Processes 83 (2022) 729–741
19. Wu, L.H., Nagatsuka, K., Nakata, K. Direct joining of oxygen-free copper and carbon-fiber-reinforced plastic by friction lap joining. Journal of Materials Science & Technology 34 (2018) 192–197.
20. Zhu XK, Chao YJ (2002) Effects of temperature-dependent material properties on welding simulation. Comput Struct 80 (11):967–976. https://doi.org/10.1016/S0045-7949(02)00040-8

Figures

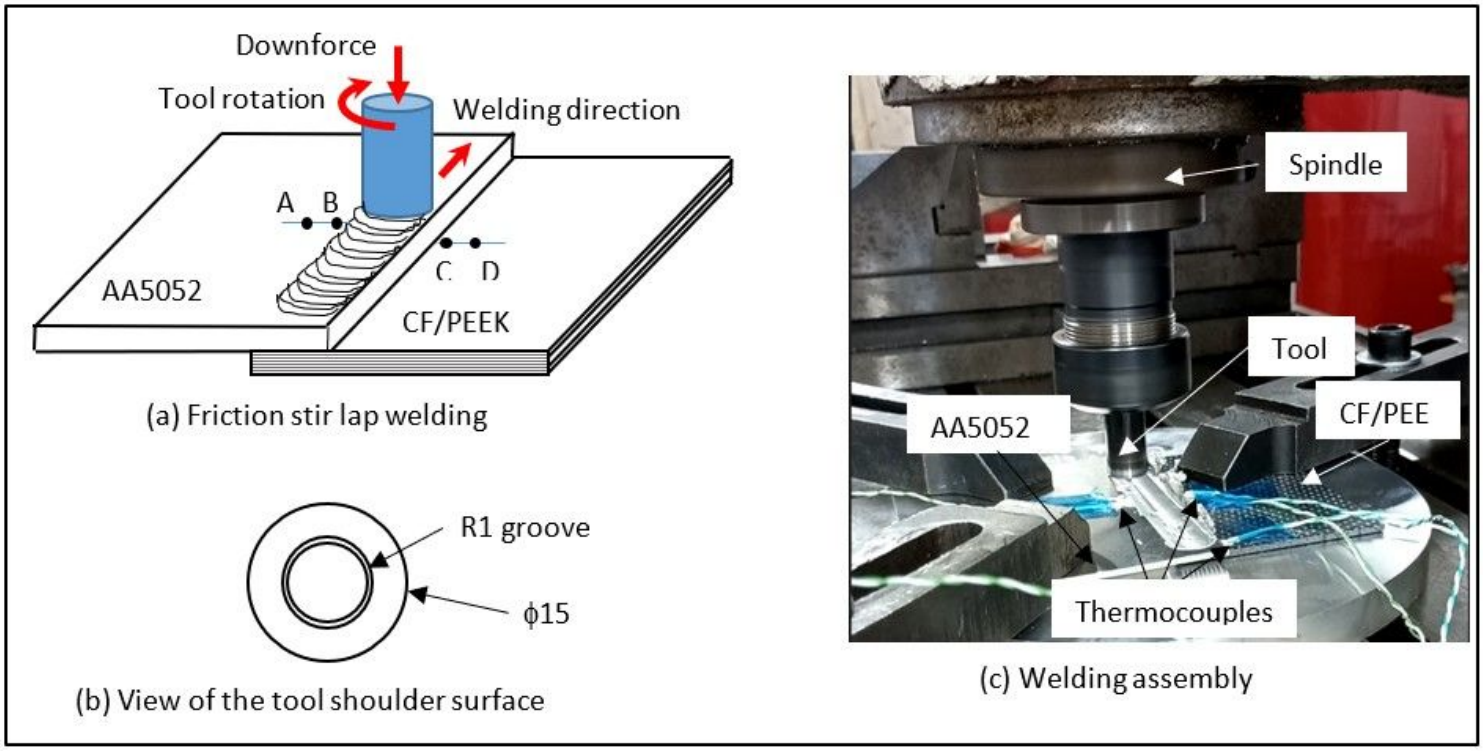

Figure 1

Different views of friction lap welding setup

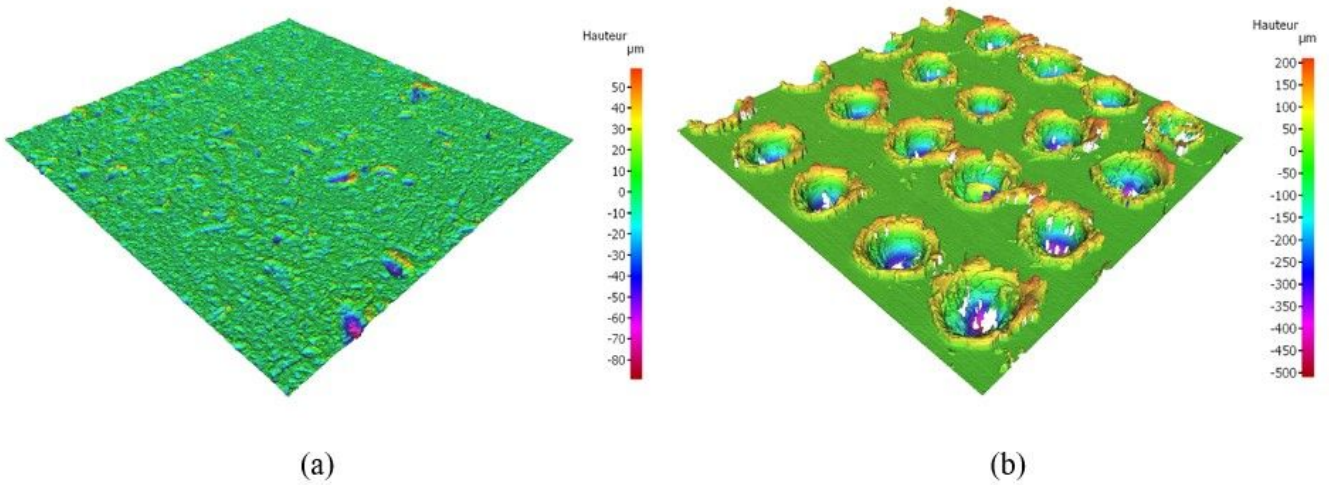

Figure 2

Surface textures of aluminum sheets with sand-blasting, (a) and engraved dots, (b). Area shown is 4x4 mm^2.

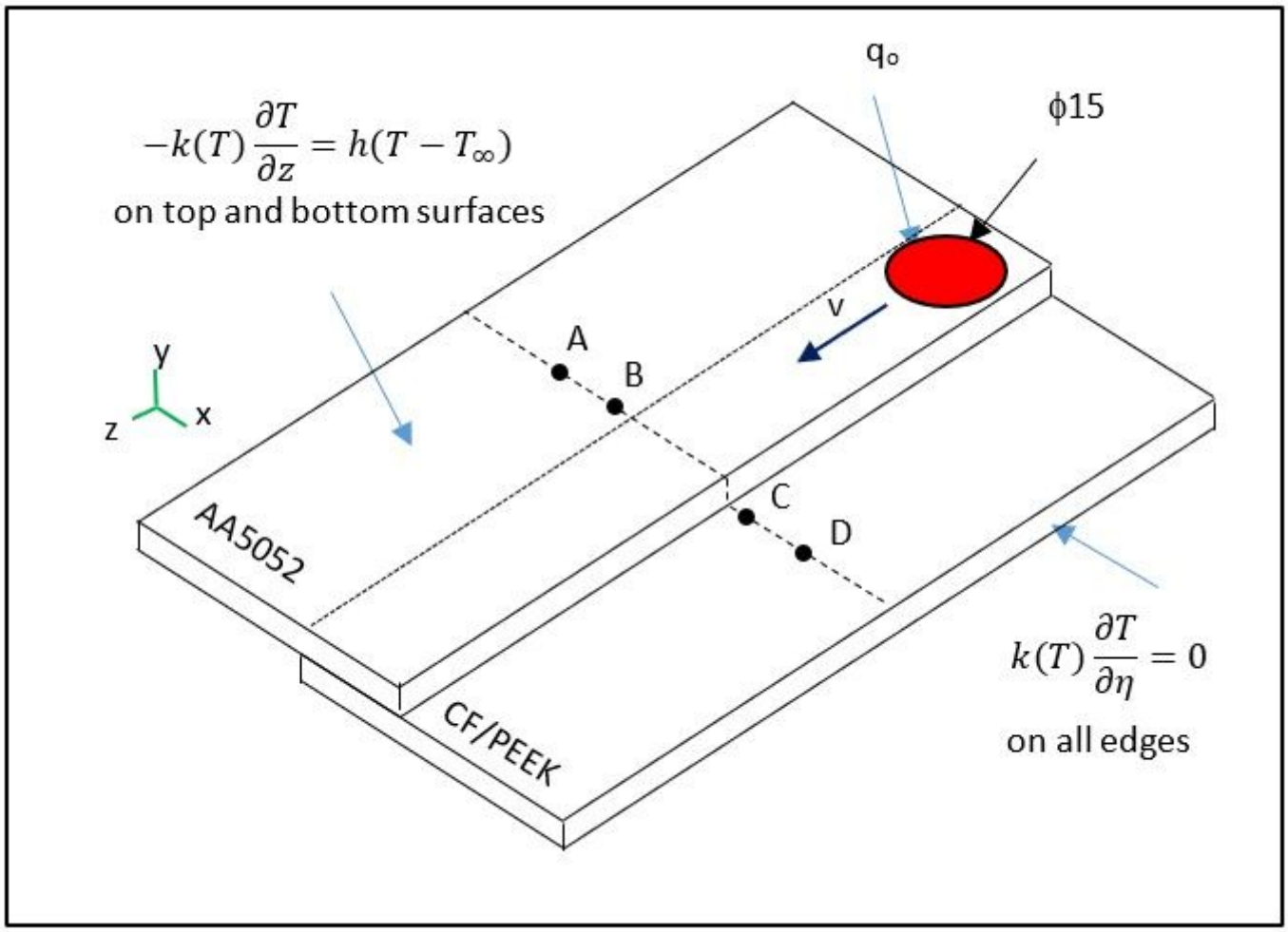

Figure 3

Numerical model of the heat conduction problem (not to scale).

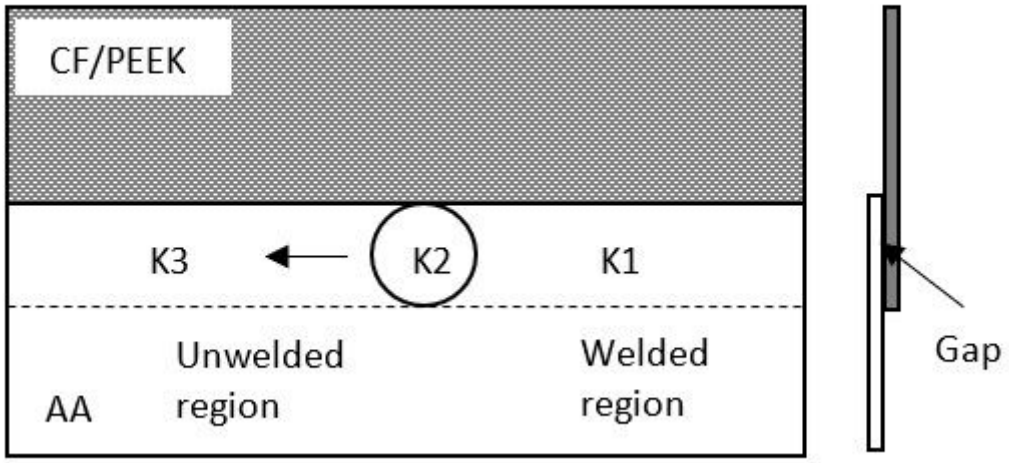

Figure 4

Definition of gap conductance in the numerical model.

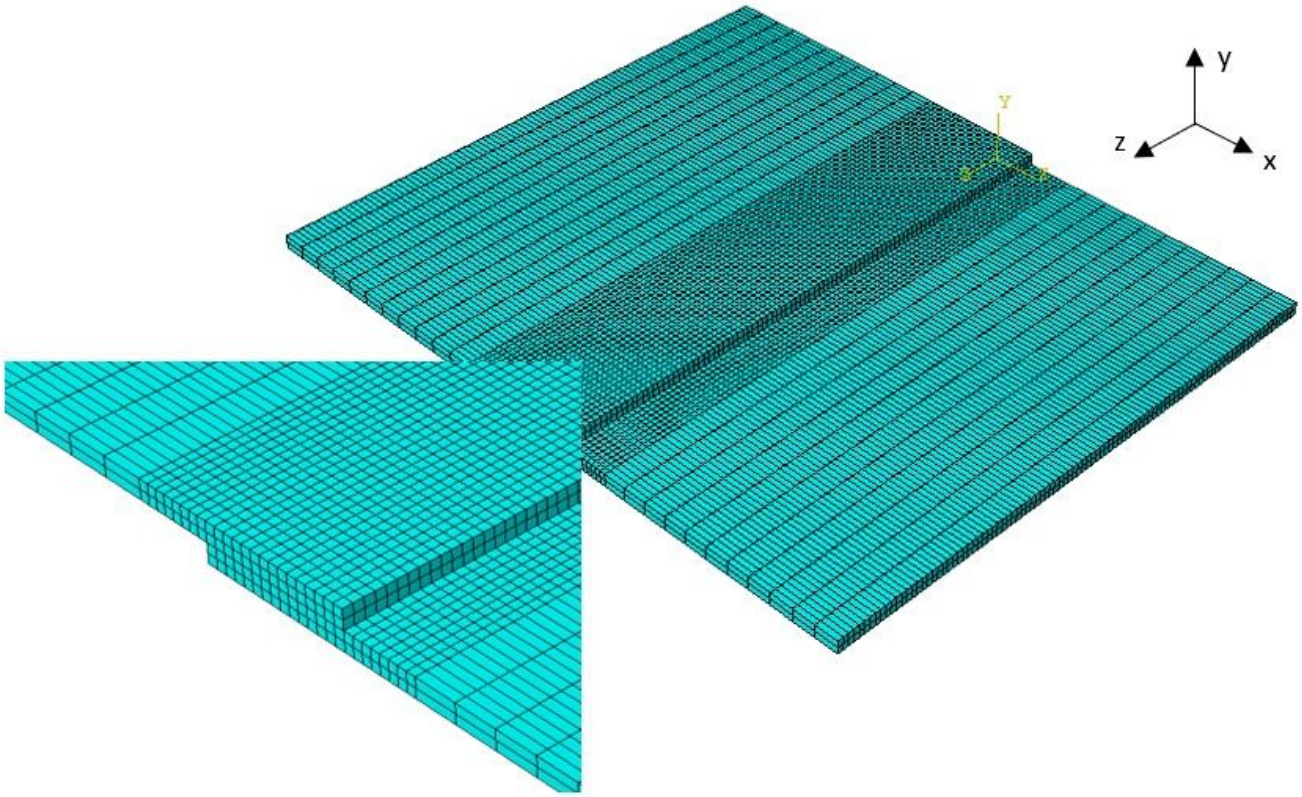

Figure 5

Discretized numerical model showing mesh size in the lap joint and surrounding regions.

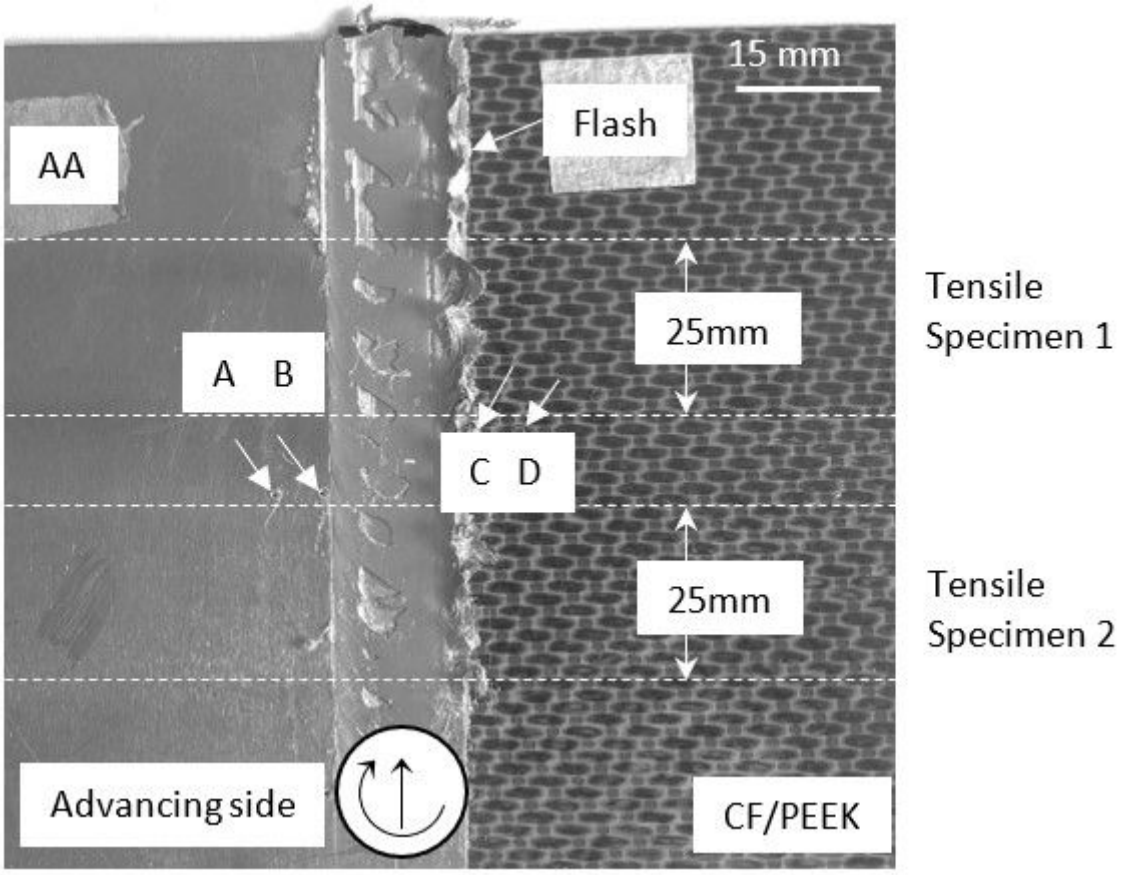

Figure 6

Appearance of the weld line for condition 7 in Table 1 (spindle speed of 1090 rpm).

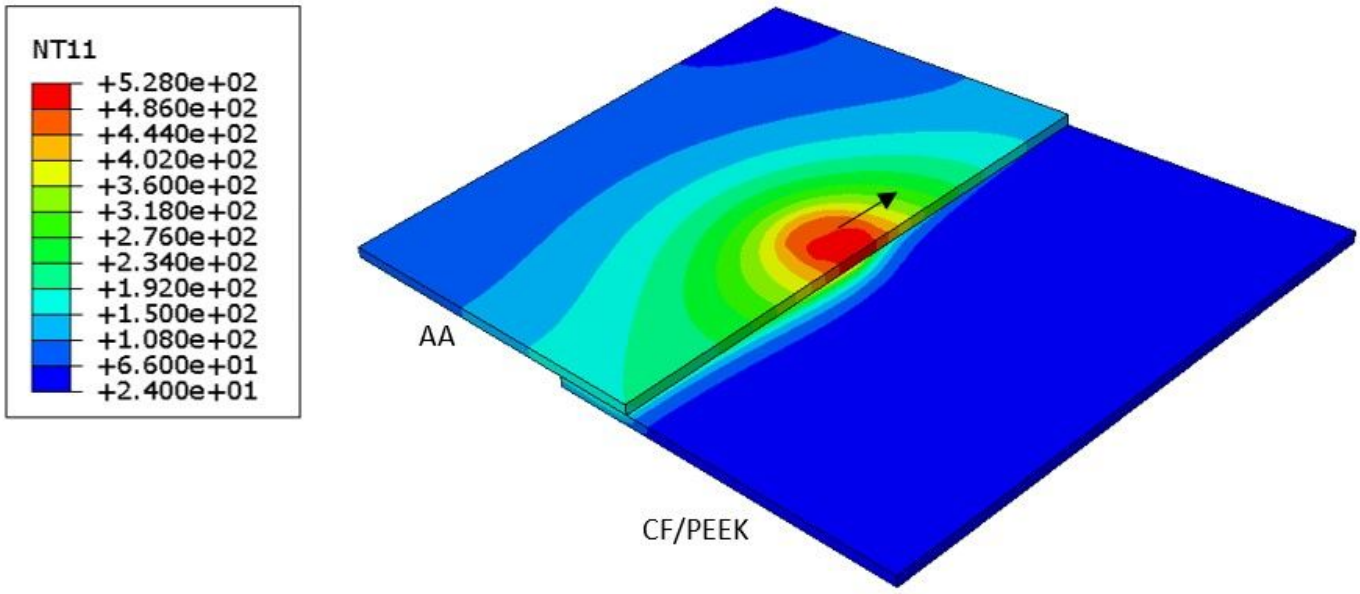

Figure 7

Temperature distribution in the lap joint for run 3 (rotational speed of 949 rpm) after 60 seconds.

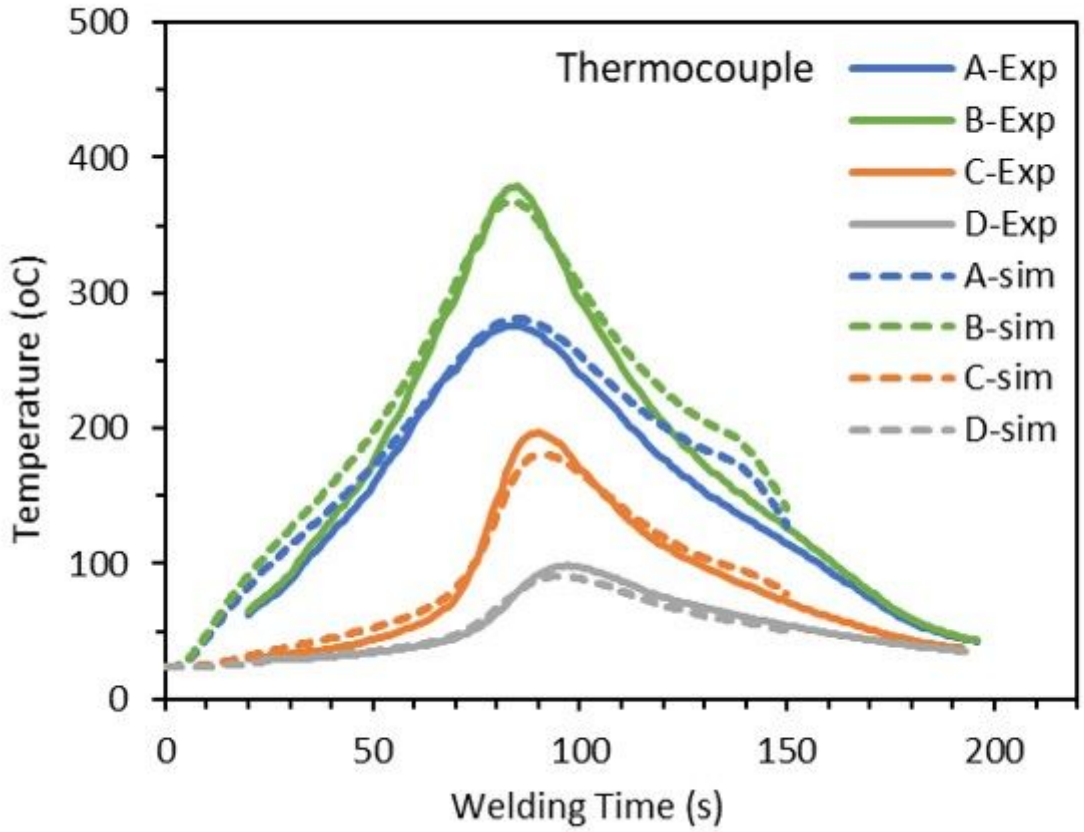

Figure 8

Measured and simulated temperature histories at thermocouple locations for welding condition 3.

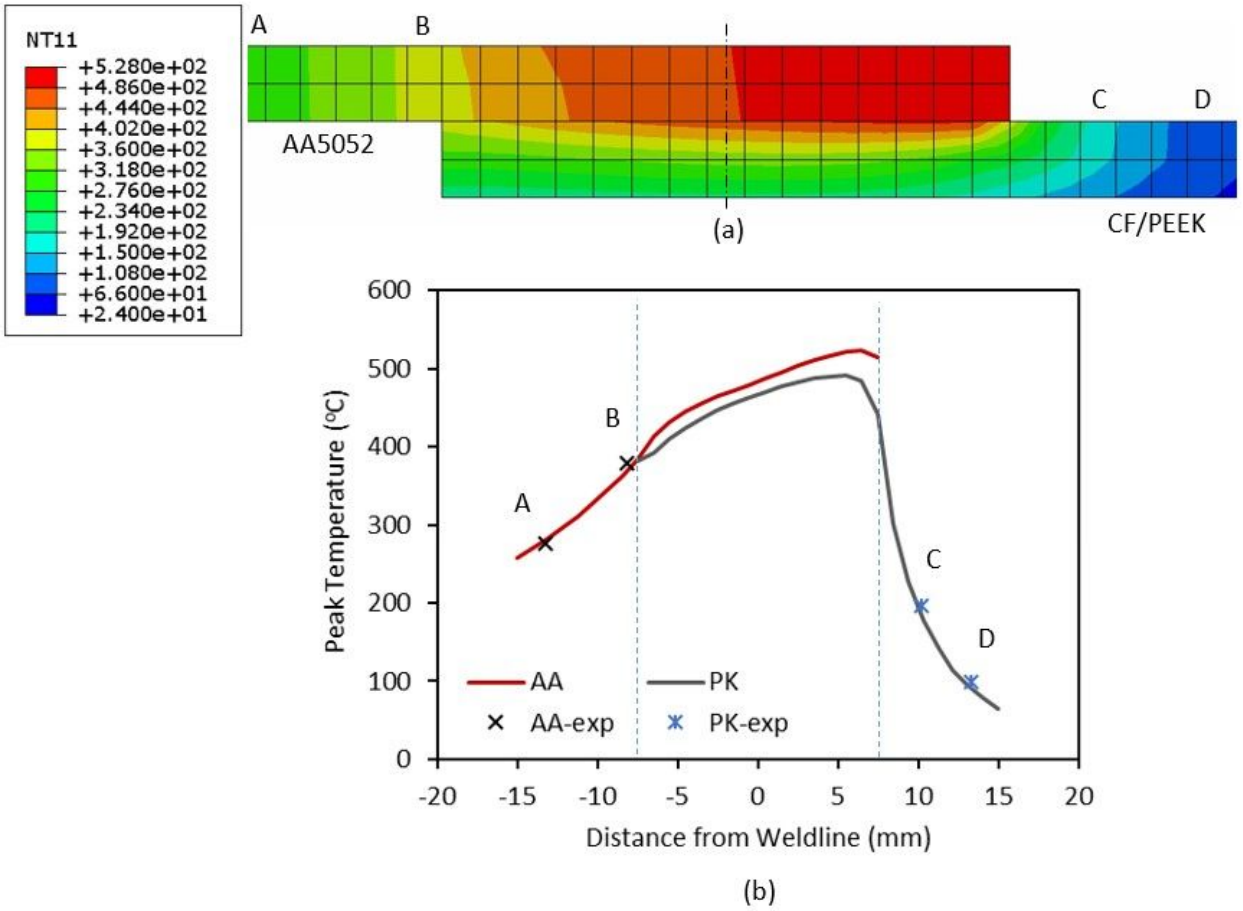

Figure 9

(a) Temperatures at the cross section of the lapjoint at time = 60 seconds, (b) measured and simulated peak temperatures at the top surfaces of AA and CF/PEEK across the weld line for welding condition 3.

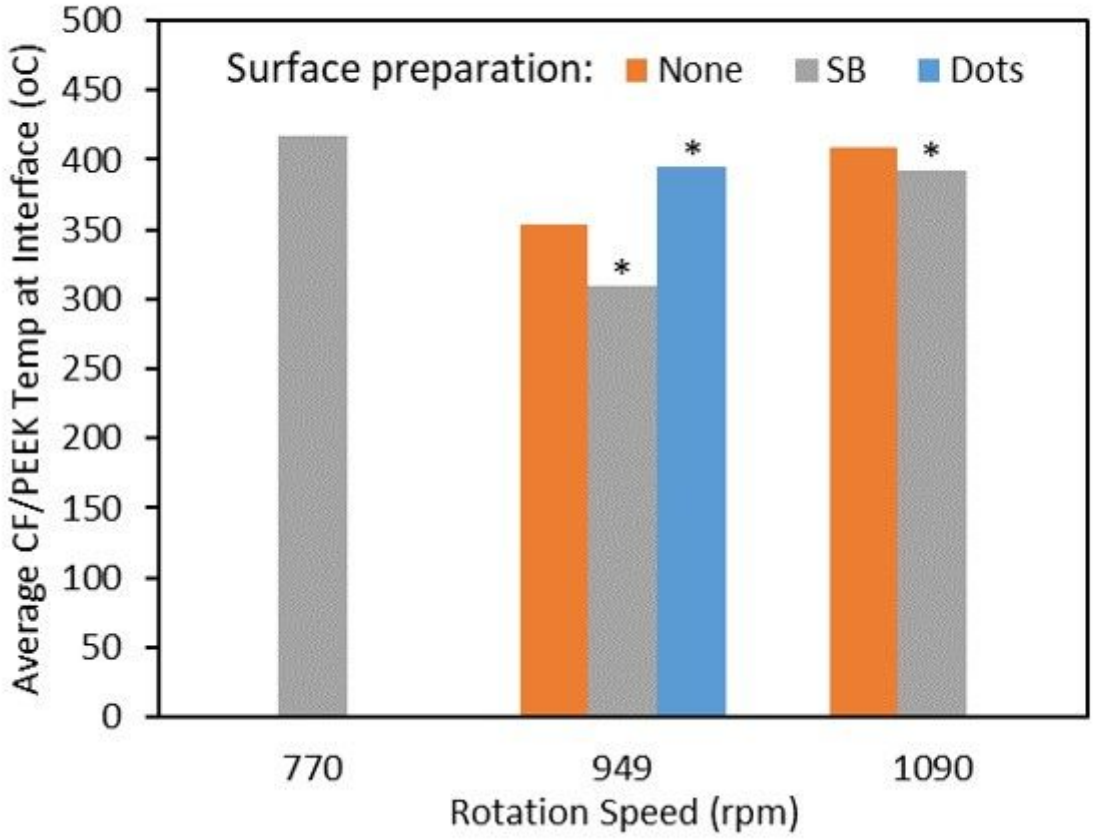

Figure 10

Correlation between simulated CF/PEEK average interface temperature and tool rotation speed. Bars with asterisks indicate a successful joint.

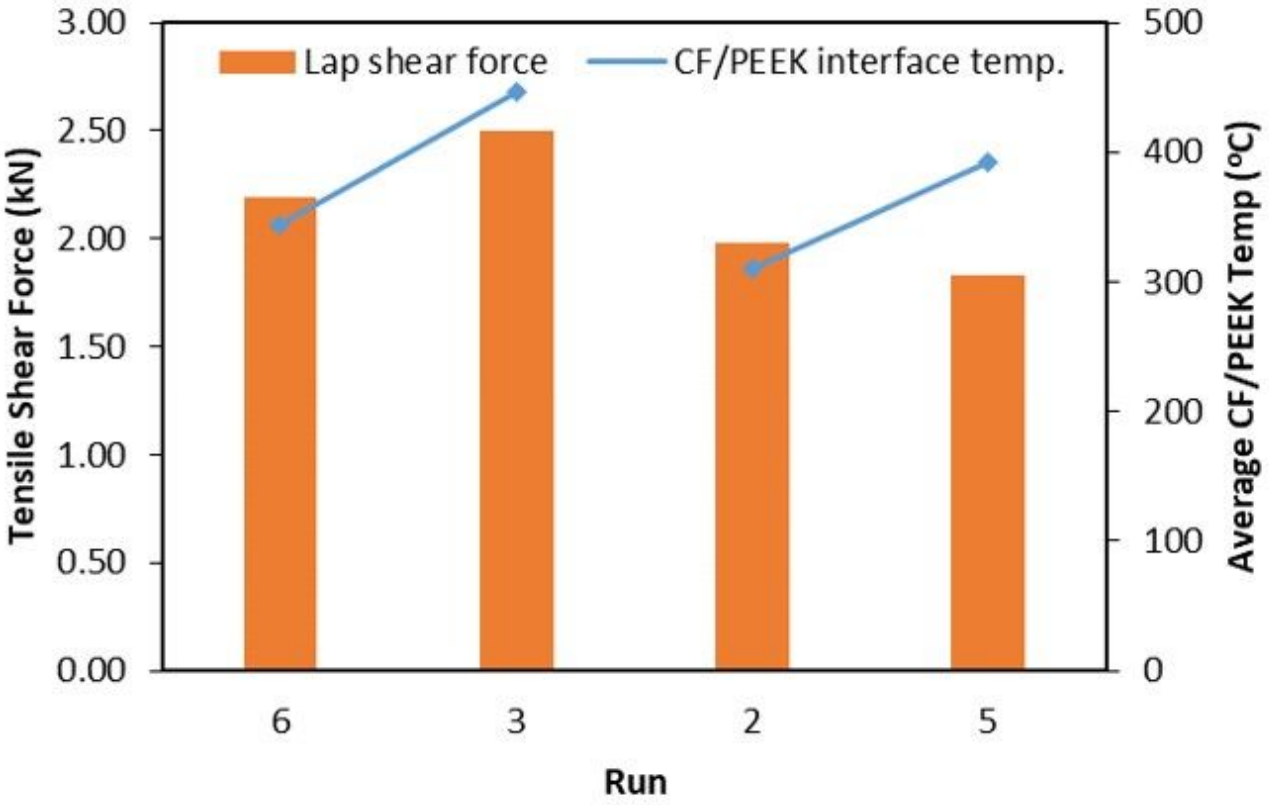

Figure 11

Correlation between the average lap shear force and average CF/PEEK interface temperature for runs which produced a joint.

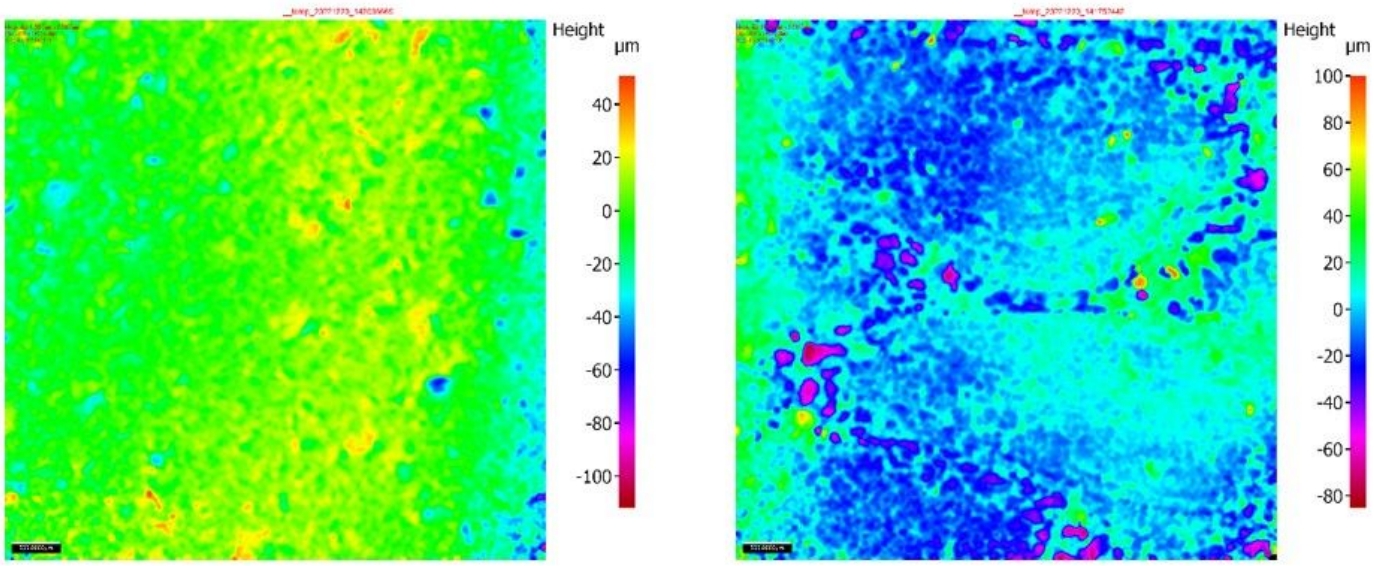

Figure 12

Surface texture of sandblasted AA and CF/PEEK lap joint after separation, AA on the left and CF/PEEK on the right.

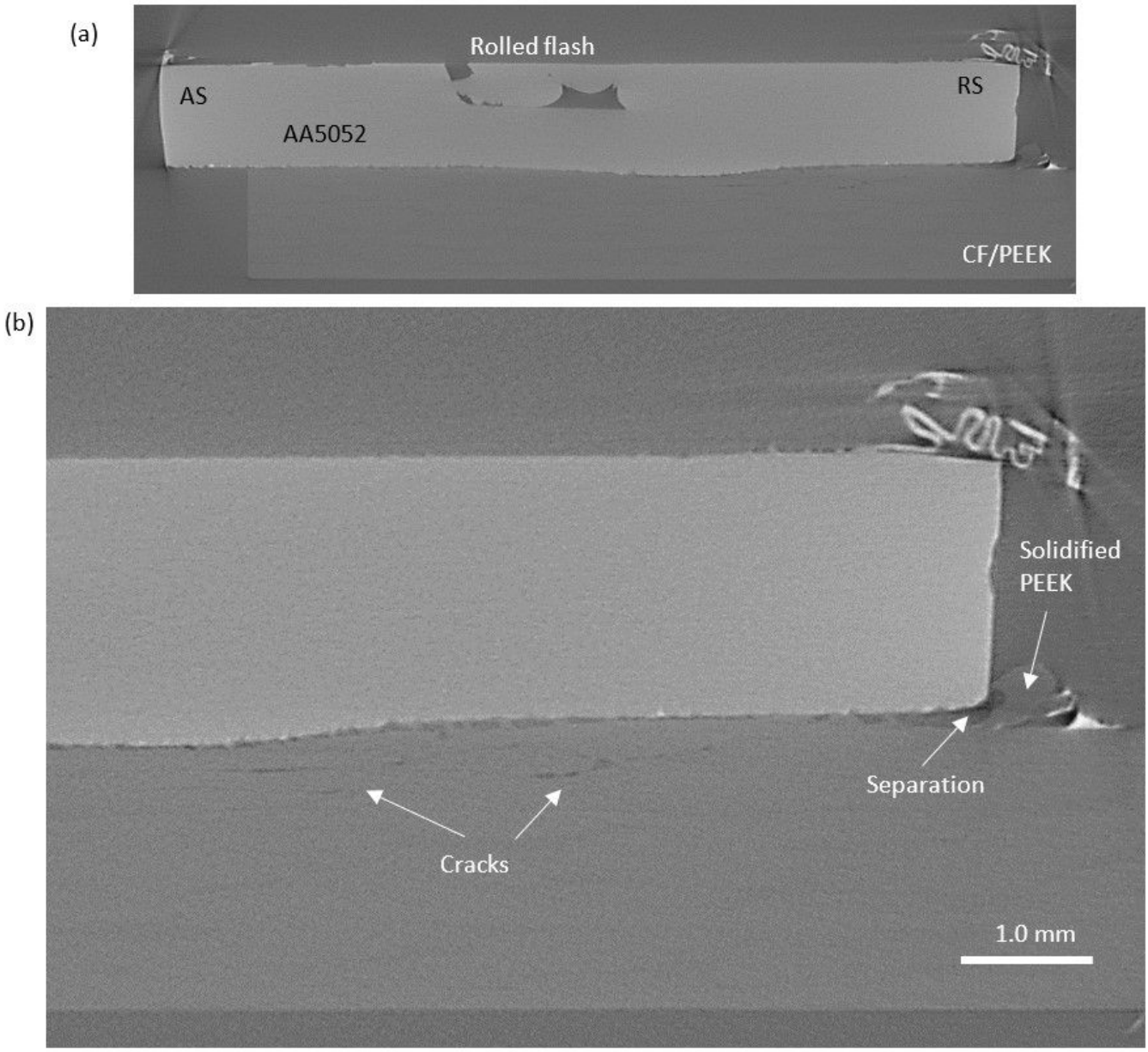

Figure 13

X-ray scan of the cross section of the joint with sand blasted AA surface (condition 2).

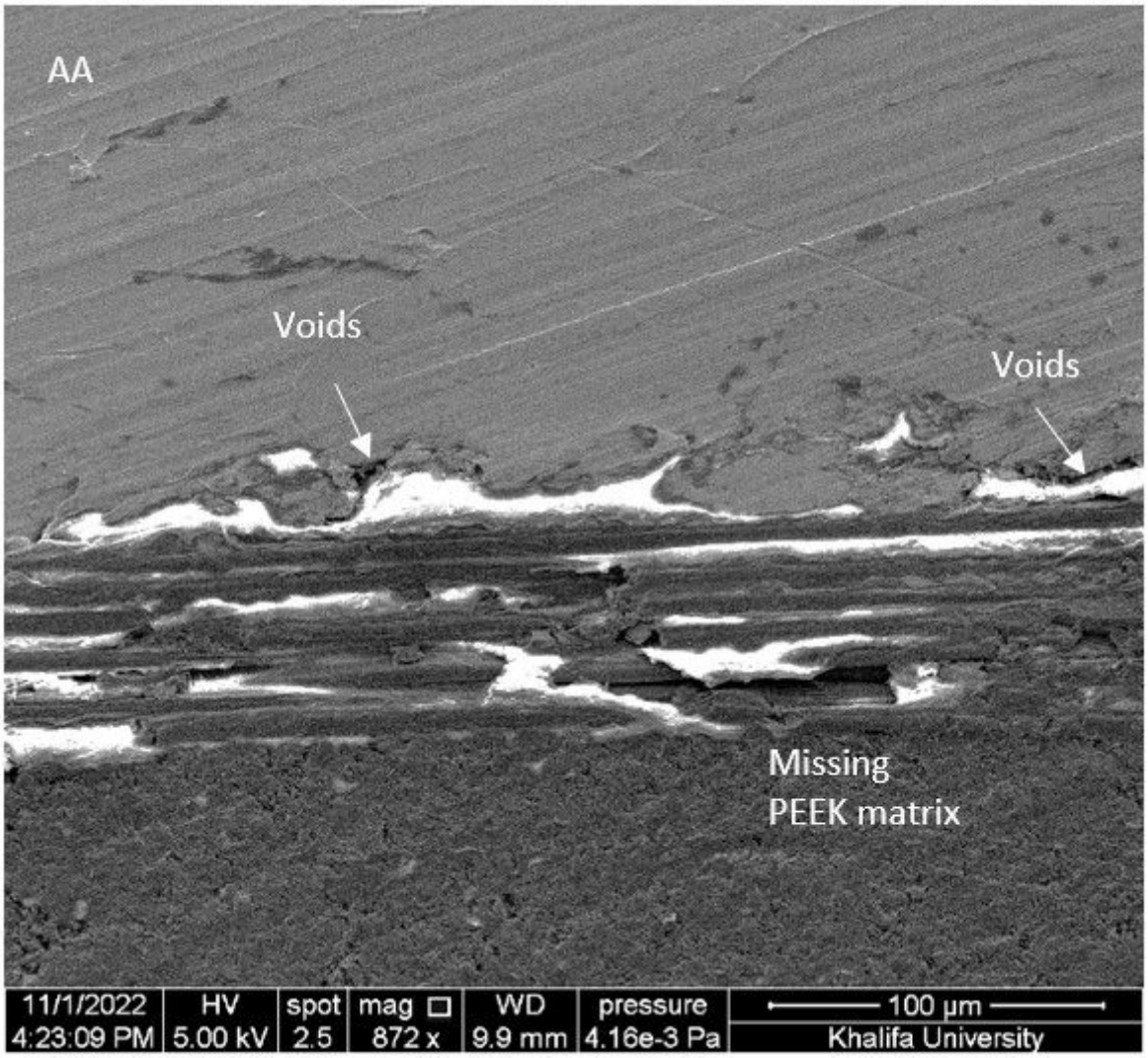

Figure 14

SEM micrograph of sandblasted lap joint interface (run 2).

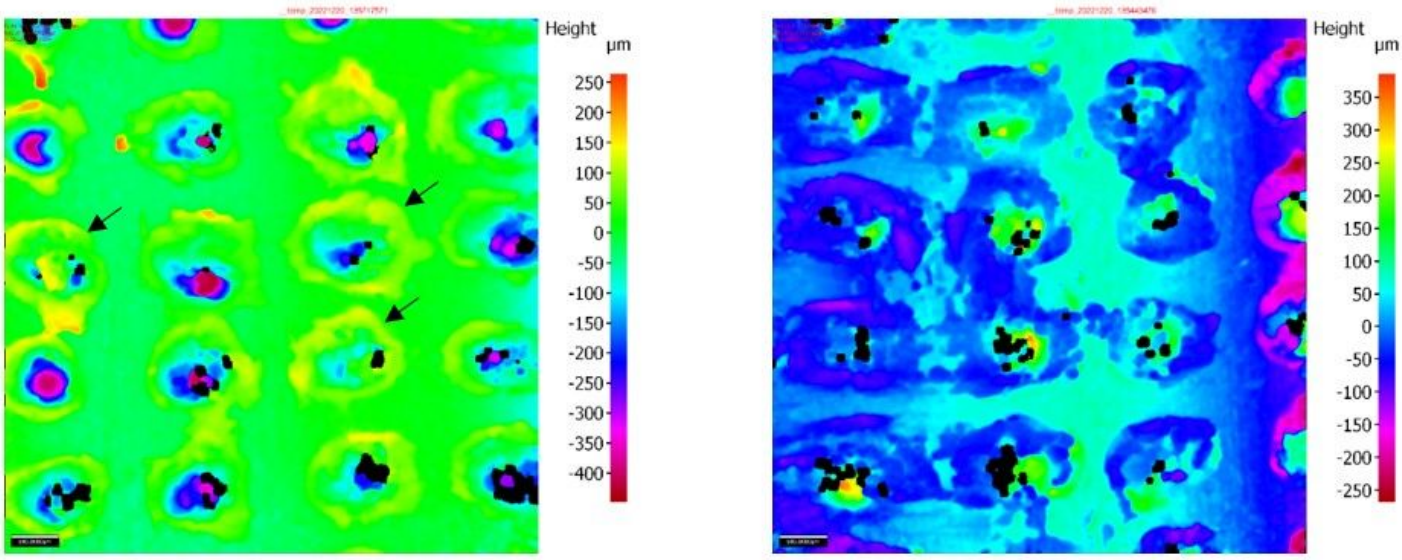

Figure 15

Surface texture of dot engraved lap joint after separation, AA on the left and CF/PEEK on the right.

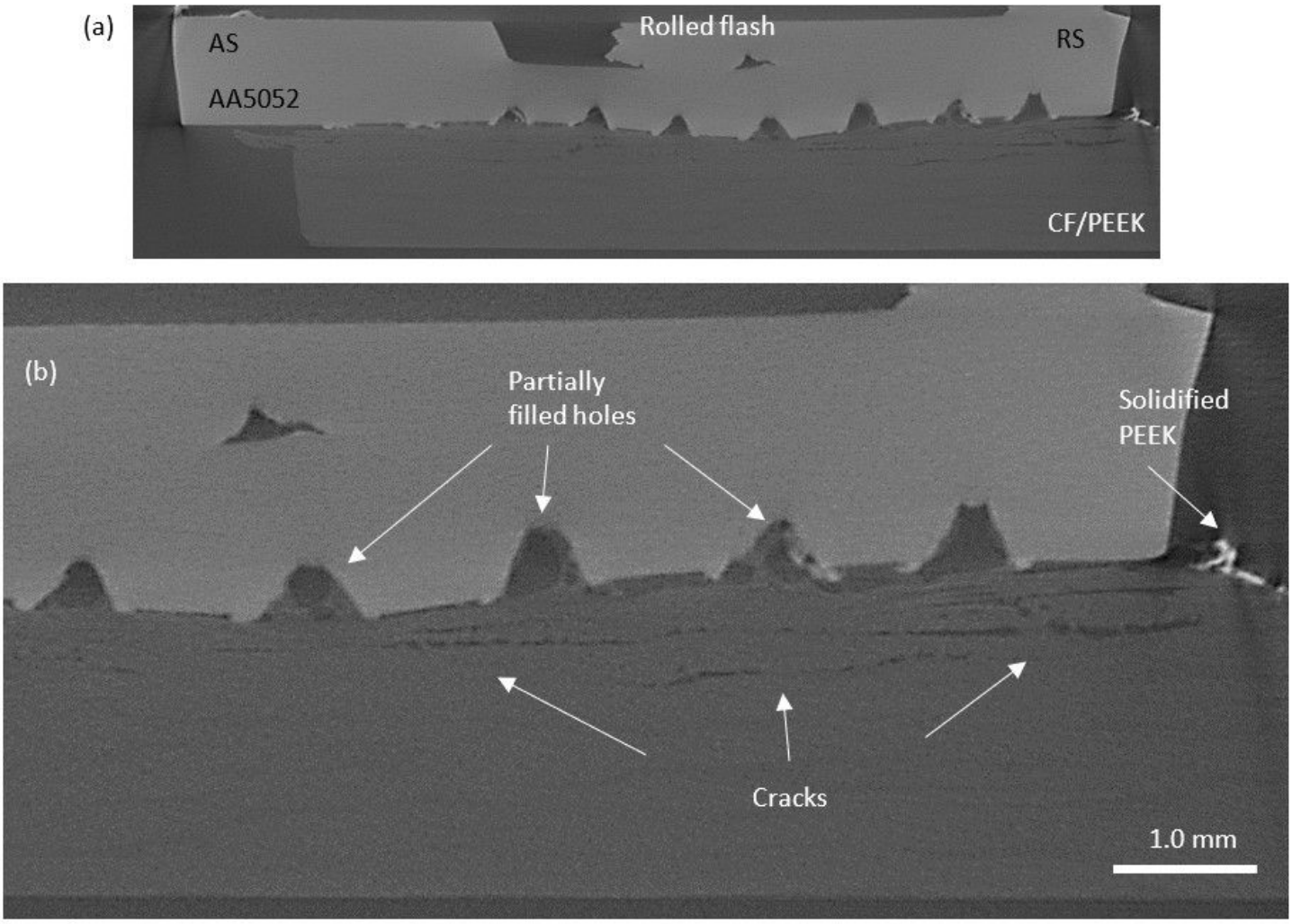

Figure 16

X-ray scan of the cross section of the joint with sand blasted AA surface (condition 3).

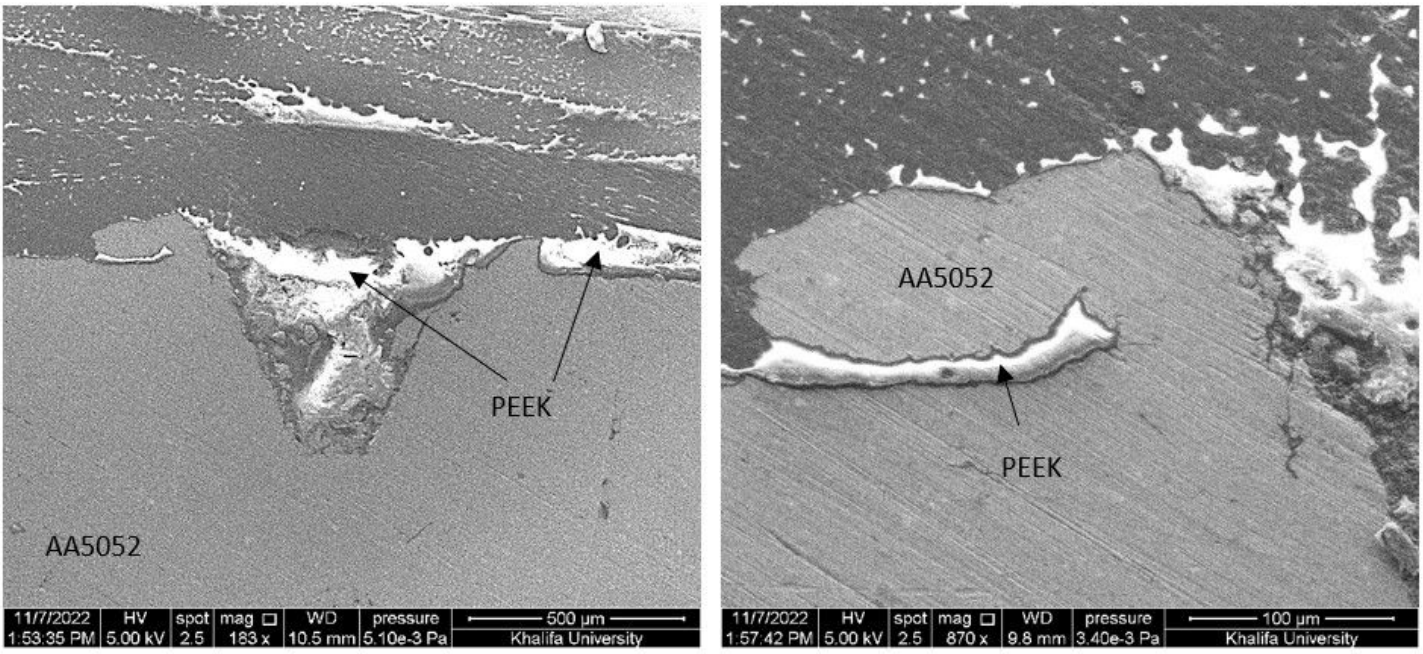

Figure 17

SEM of dot engraved lap joint interface.